JACS Au
AN OPEN ACCESS JOURNAL OF THE AMERICAN CHEMICAL SOCIETY

pubs.acs.org/jacsau
Article

^{18}F-Fluorination of Nitroimidazolyl-Containing Sultone: A Direct Access to a Highly Hydrophilic Radiotracer for High-Performance Positron Emission Tomography Imaging of Hypoxia

Clémence Maingueneau, Anne-Elodie Lafargue, Stéphane Guillouet, Fabien Fillesoye, Thanh T. Cao Pham, Bénédicte F. Jordan, and Cécile Perrio*

Cite This: *JACS Au* 2024, 4, 3248–3257

Read Online

ACCESS | Metrics & More | Article Recommendations | Supporting Information

ABSTRACT: Hypoxia, characterized by nonphysiological levels of oxygen tension, is a key phenomenon common to the majority of malignant tumors with poor prognosis. Many efforts have been made to develop hypoxia imaging for diagnosis, staging, and monitoring of diseases, as well as for evaluating therapies. PET Imaging using ^{18}F-fluoronitroimidazoles (i.e., [^{18}F]FMISO as a lead radiotracer) has demonstrated potential for clinical investigations, but the poor contrast and prolonged acquisition times (>2.5 h) strongly limit its accuracy and routine developments. Here, we report an original [^{18}F]fluoronitroimidazole bearing a sulfo group ([^{18}F]FLUSONIM) that displays highly hydrophilic properties and rapid clearance, providing high-performance hypoxia specific PET imaging. We describe the synthesis and radiosynthesis of [^{18}F]FLUSONIM, its *in vivo* preclinical evaluation by PET imaging in healthy rats and a rhabdomyosarcoma rat model, as well as its radiometabolization and histological studies. [^{18}F]FLUSONIM was prepared in a single step by high yielding radiofluorination of a sultone precursor, highlighting the advantages of this new radiolabeling approach not yet explored for radiopharmaceutical development. PET imaging experiments were conducted by systematically comparing [^{18}F]FLUSONIM to [^{18}F]FMISO as a reference. The overall results unequivocally demonstrate that the developed radiopharmaceutical meets the criteria of an ideal candidate for hypoxia PET imaging—rapid and efficient radiosynthesis, total stability, exclusive urinary elimination, high specificity for hypoxic regions, unprecedented tumor/background ratios, short acquisition delays (<60 min), and promising potential for further preclinical and clinical applications.

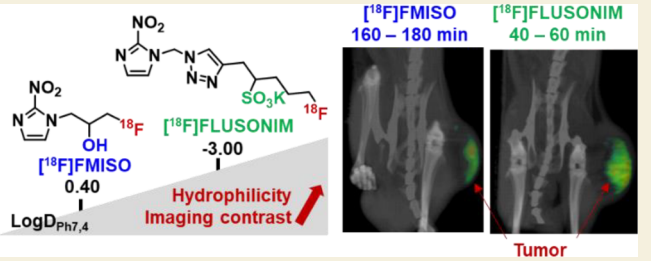

KEYWORDS: *hypoxia imaging, positron emission tomography, fluorine-18, nitroimidazole, radiotracer, cancer, rhabdomyosarcoma*

INTRODUCTION

Hypoxia is an important hallmark of solid tumors and plays a critical role in various cellular and physiologic processes, including cell proliferation, angiogenesis, tumor invasion, and metastasis.[1,2] It has also been shown to contribute to chemo- and radiotherapy resistance associated with poor clinical prognosis.[3] It is well recognized that knowledge of the location, extent, and reduction of hypoxia can provide valuable information for adapting treatments and potentially improving therapeutic outcomes, especially in radiotherapy and dose-painting approaches.[4−6] For many years, positron emission tomography (PET) has proven to be a suitable noninvasive *in vivo* imaging technique for detecting hypoxic tumor regions.[7,8] Hypoxia clinical PET imaging is mainly based on the use of 2-nitroimidazole containing radiopharmaceuticals, e.g., ^{18}F-labeled fluoromisonidazole ([^{18}F]FMISO) that remains the reference radiotracer for this purpose due to its well-establised prognostic potential.[8,9−12] Nitroimidazolyl radiotracers have been shown to penetrate cells by passive diffusion and then undergo a two-step reduction process, with the first step being reversible when oxygen is present. Thus, the radiotracers stand out unchanged from normal cells, whereas they become irreversibly trapped in hypoxic cells due to the *in situ* conjugation of their reduced forms with enzymes and proteins. Although [^{18}F]FMISO has been extensively studied in several preclinical and clinical studies for cancer imaging, its suitability is limited due to slow clearance, low tumor-specific accumulation, and nonspecific washout. These factors result in poor imaging contrast and necessitate long delays (>3 h) post-injection for image acquisition. Images typically remained of poor quality and required complex data processing for analysis.[13] A variety of 2-nitroimidazole analogues with different clearance and hydrophilicity characteristics, such as [^{18}F]fluoroazomycin arabino-

Received: June 25, 2024
Revised: July 19, 2024
Accepted: July 19, 2024
Published: August 2, 2024

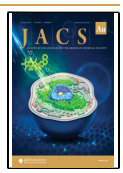

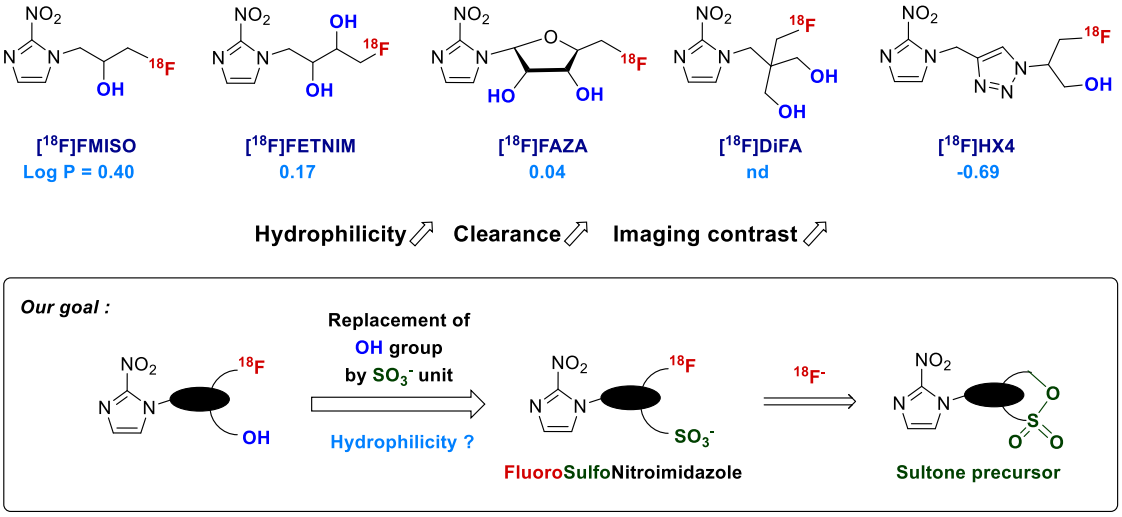

Figure 1. Usual 2-nitroimidazole-based radiopharmaceuticals for clinical PET imaging of hypoxia and the rationale for the development of a new hydrophilic sulfo analogue.

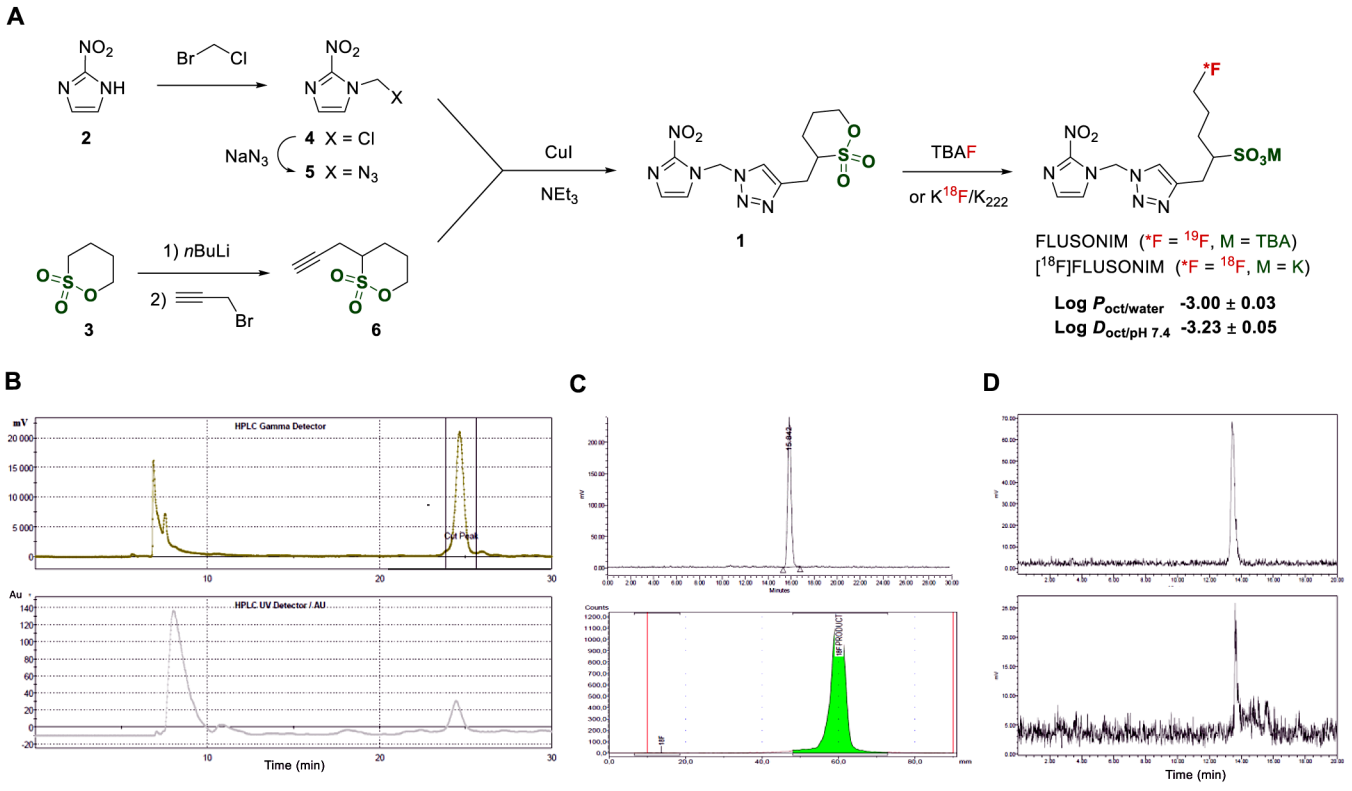

Figure 2. (A) Synthesis and radiosynthesis of the investigated FLUSONIM; (B) preparative HPLC (up, γ trace; down, UV trace) for [^{18}F]FLUSONIM purification at the end of radiosynthesis; (C) quality control of [^{18}F]FLUSONIM ready for injection (up, RadioHPLC analysis; down, radio TLC analysis); (D) analytical RadioHPLC for stability studies of [^{18}F]FLUSONIM in plasma (up, *in vitro* after incubation for 150 min at 37 °C in plasma; down, *ex vivo* after extraction of blood 150 min post-injection).

side ([^{18}F]FAZA), [^{18}F]fluoroerythronitroimidazole ([^{18}F]-FETNIM), [^{18}F]fluoroetanidazole ([^{18}F]FETA), [^{18}F]-nitroimidazolyl-*N*-(pentafluoropropyl)acetamide ([^{18}F]EF5), [^{18}F]flortanidazole ([^{18}F]HX4), and more recently [^{18}F]DiFA, have been developed in an attempt to overcome these disadvantages (Figure 1). Among these, [^{18}F]HX4[14−22] and [^{18}F]DiFA[23,24] offered higher contrast images compared to those obtained with [^{18}F]FMISO, due to their rapid clearance resulting from better water solubility properties. Also importantly with [^{18}F]DiFA, image acquisition delays post-injection could be significantly reduced compared to those required with [^{18}F]FMISO, and clinical developments remained promising. As a consequence, the hypothesis that greater hydrophilicity leads to better imaging quality was confirmed. Thus, the development of new ^{18}F-nitroimidazole derivatives with superior hydrophilic properties was needed in order to achieve high-performance hypoxia imaging for accurate and routine clinical developments.

https://doi.org/10.1021/jacsau.4c00546
JACS Au 2024, 4, 3248−3257

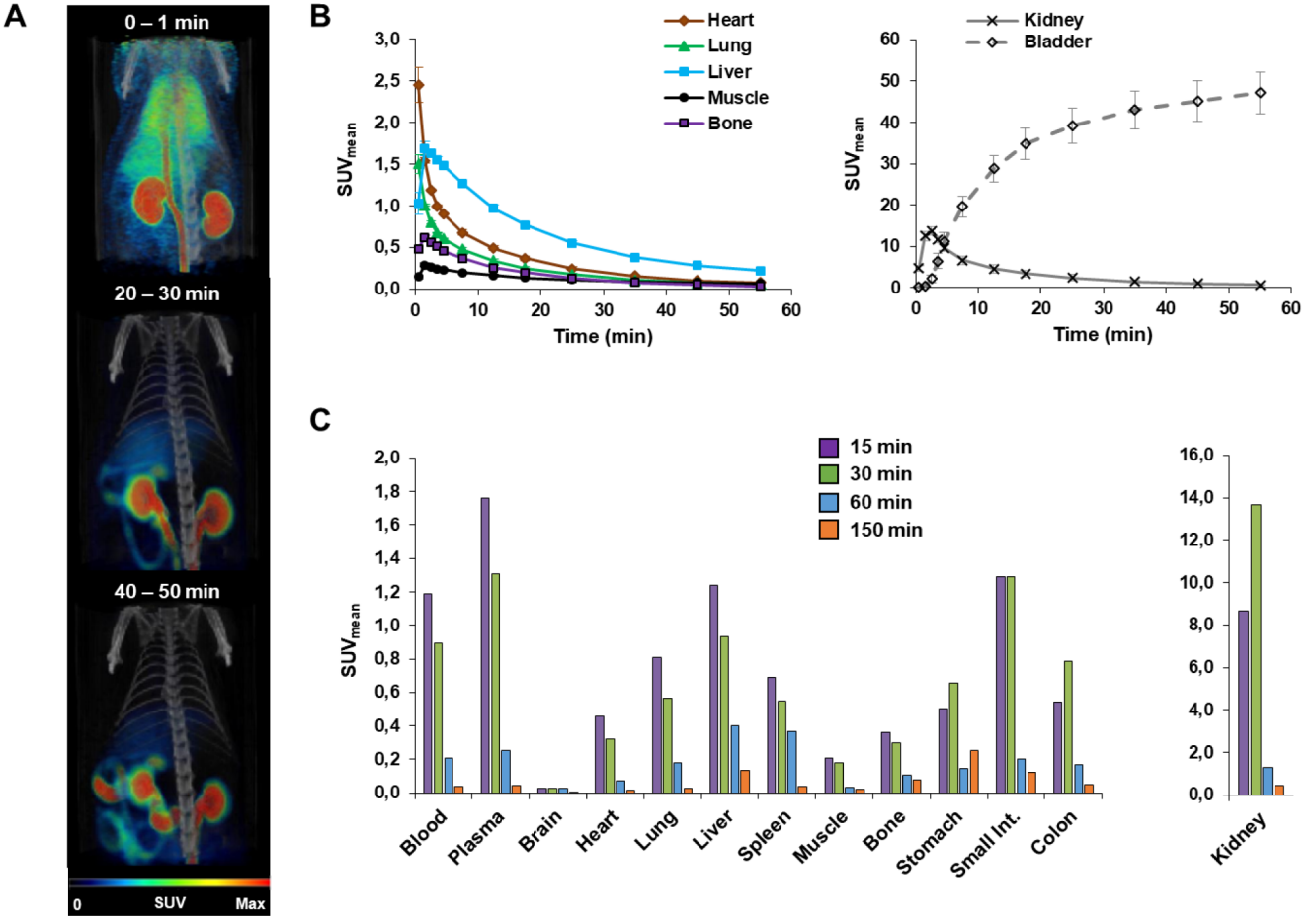

Figure 3. Biodistribution by PET imaging of [^{18}F]FLUSONIM in the main organs after i.v. injection in healthy rats. (A) Fused PET/CT images. (B) Time−activity curves. (C) Repartition at 15, 30, 60, and 150 min.

With its convenient 109.7 min half-life and almost exclusive low-energy β^+ decay (635 keV), fluorine-18, in its no-carrier-added, nucleophilic fluoride ([^{18}F]F$^-$) form, remains one of the most practical nuclides currently in use for clinical PET imaging.[25,26] An important feature in the development of ^{18}F-radiotracers for clinical applications is the ability to perform the radiosynthesis in a one-step, fully automated, high-yielding, and cGMP-compliant process, and in the shortest possible time. Among the arsenal of available radiofluorination reactions using [^{18}F]F$^-$ anion, aliphatic nucleophilic substitution of alkylsulfonates (triflate, tosylate, mesylate, or nosylate) presents the advantage of being a metal-free, user-friendly method, and serves for the preparation of main radiopharmaceuticals used in clinical settings, such as [^{18}F]FDG, [^{18}F]FMISO, and their analogues. We previously reported, for the first time, the ring opening of sultone by [^{18}F]fluoride as the cyclic version of sulfonate displacement.[27] This reaction was demonstrated to afford ^{18}F-fluorosulfonic acid salts in high yields under mild heating conditions without any additives. Furthermore, the introduction of a sulfo group into organic compounds is commonly used to enhance their hydrophilicity.[28] We then aimed to develop an ^{18}F-fluoronitroimidazole analogue bearing a sulfo group as a potential highly hydrophilic radiotracer for hypoxia PET imaging (Figure 1). The latter can be easily prepared from a nitroimidazole precursor bearing a sultone moiety. We report here the synthesis, radiosynthesis, and hydrophilic properties of the designed radiopharmaceutical, as well as results for *in vivo* stability, biodistribution, and specificity for hypoxia by preclinical PET imaging. We chose a rhabdomyosarcoma model, previously well characterized as a hypoxic tumor and used for [^{18}F]FMISO and [^{18}F]HX4 evaluation.[13] We then compared [^{18}F]FLUSONIM to [^{18}F]FMISO, investigating the uptake of the radiotracer over time and determining the tumor-to-background ratios. We also performed histological, immunostaining, and autoradiography experiments to correlate with the *in vivo* experiment results.

RESULTS AND DISCUSSION

Design, Synthesis, and Radiolabeling

The goal was to investigate the impact of replacing a hydroxyl group in the ^{18}F-nitroimidazole radiotracers with a charged sulfo function for PET imaging. We then designed FLUSONIM (for FLUoroSulfONItroiMidazole) based on the structure of HX4 characterized by the lowest Log *p*-value of −0.69 reported so far.[29] FLUSONIM incorporated a metabolically stable 1,2,3-triazole moiety between the 2-nitroimidazole group and the fluorosulfonic acid salt entity (Figure 2A). Its radiolabeling was planned as a one-step process by nucleophilic radiofluorination of the sultone precursor **1** prepared from commercially available 2-nitroimidazole **2** and butane sultone **3**. 2-Nitroimidazole **2** was converted to the chloro derivative **4**[30] and then to the azido compound **5** by alkylation with chlorobromethane followed by substitution with sodium azide. The treatment of butane sultone **3** with *n*-butyl lithium, followed by propargyl bromide, led to

https://doi.org/10.1021/jacsau.4c00546
JACS Au 2024, 4, 3248−3257

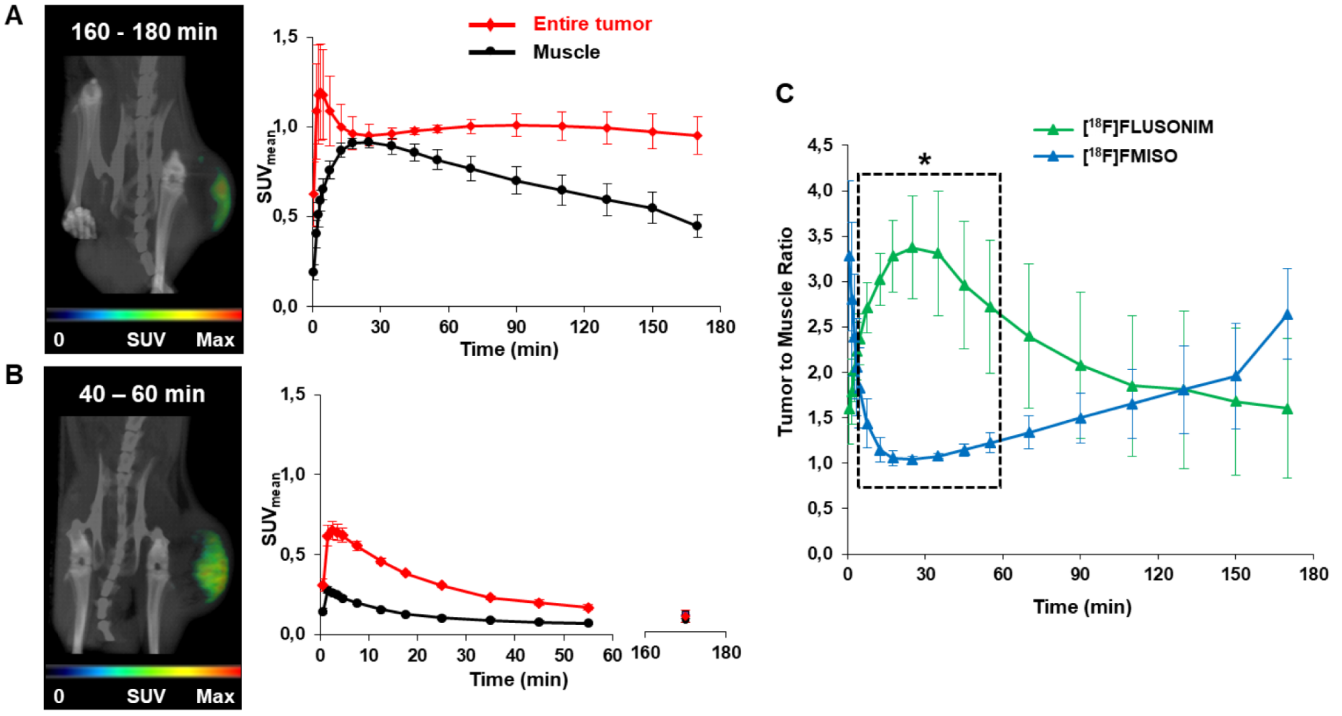

Figure 4. PET Imaging in the rhabdomyosarcoma model ($n = 8$). (A) Fused PET/CT images hidden from elimination organs and time activity curves for [^{18}F]FMISO. (B) Fused PET/CT images and time activity curves for [^{18}F]FLUSONIM. (C) Tumor-to-muscle ratio results for [^{18}F]FMISO and [^{18}F]FLUSONIM (*$P < 0.05$).

alkynylsultone **6**.[31] The Cu-catalyzed cycloaddition reaction of alkynylsultone **6** with azide **5** afforded sultone precursor **1**. The fluorination of sultone **1** to FLUSONIM was carried out with either TBAF or KF in the presence of kryptand K_{222} (Kryptofix) quantitatively. The radiosynthesis of [^{18}F]FLUSONIM was performed by radiofluorination of sultone **1** with a classically prepared $K^{18}F/K_{222}/K_2CO_3$ complex in acetonitrile at 110 °C for 15 min. Conversions were above 90%. Purification by semi-preparative HPLC using a 1:9 ethanol/NaH_2PO_4 (10 mM) mixture as an eluent afforded formulated, ready-to-injection [^{18}F]FLUSONIM (Figure 2B). The fully automated process provided [^{18}F]FLUSONIM with an activity yield of 49 ± 8% (not decay corrected, calculated from cyclotron produced [^{18}F]fluoride, $n > 12$) in under 45 min from end-of-bombardment (EOB). The quality control revealed high radiochemical purity (>99%, Figure 2C) and a molar activity of >500 GBq/μmol (13 Ci/μmol). The one-step process in addition to the easy separation of sultone precursor **1** and [^{18}F]FLUSONIM due to their high polarity differences, as well as the short total radiosynthesis time, made the production highly efficient for imaging developments.

Hydrophilicity and *In Vitro* Stability

[^{18}F]FLUSONIM exhibited octanol/water and octanol/buffer (pH 7.4) partition coefficient values of Log $P = -3.00 \pm 0.03$ and and Log $D = -3.23 \pm 0.05$, respectively (Figure 2A). These values were much lower than those of all other radiotracers developed so far, including the structurally closest [^{18}F]HX4 (Log P of −0.69),[14] and confirmed the highly hydrophilic character of [^{18}F]FLUSONIM, in accordance with the presence of the sulfo group. RadioHPLC and radioTLC analyses showed that [^{18}F]FLUSONIM was recovered totally unchanged after incubation for 180 min at 37 °C, both in the formulation medium and in plasma (Figure 2D).

Biodistribution and Stability Studies in Healthy Animals

[^{18}F]FLUSONIM was first evaluated in healthy Wistar rats to assess radiotracer biodistribution, elimination, and *in vivo* stability. We performed dynamic PET imaging over 150 min, followed by microdissection at the end of the PET acquisition (Figure 3). During the initial 30 min, the radioactivity was rapidly distributed throughout the body, with the highest concentration observed in the kidneys, where the mean standard uptake values (SUV_{mean}) reached 13.5 at 30 min. The radioactivity uptake was much lower in all other organs, with the order of uptake being as follows: intestine, liver, lung, spleen, colon, stomach, heart, bone, and muscle ($SUV_{mean} < 2$). Penetration into the brain was almost nonexistent. From 60 min onward, the radioactivity levels declined dramatically in all organs, showing no retention of [^{18}F]FLUSONIM, including in the kidneys ($SUV_{mean} < 1$). The radioactivity was mostly recovered in the bladder ($SUV_{mean} \sim 45$), demonstrating a predominant route of elimination via urine rather than hepatobiliary pathways, which is in total accordance with the highly hydrophilic property of [^{18}F]FLUSONIM. At 60 min after injection, the total excretion of [^{18}F]FLUSONIM was 60% (% ID), with approximately 58% (% ID) excreted via urine and only about 2% (% ID) into the gallbladder. For comparison, at 60 min post-injection, [^{18}F]DiFA was recovered in urine and gallbladder at >62% and 32% (% ID), respectively, in EMT6 tumor-bearing mice.[23]

Thus, the overall results revealed a very rapid clearance of [^{18}F]FLUSONIM from normal tissues and the blood pool, making it highly distinct from [^{18}F]FMISO but similar to [^{18}F]HX4 and [^{18}F]DiFA. *In vivo* stability of [^{18}F]FLUSONIM was also confirmed by radioHPLC analysis of serum samples collected 150 min post-injection. Intact [^{18}F]FLUSONIM was recovered as the sole radioactive product detected (Figure 2D), demonstrating that no metabolism occurred. The high *in vivo*

https://doi.org/10.1021/jacsau.4c00546
JACS Au 2024, 4, 3248−3257

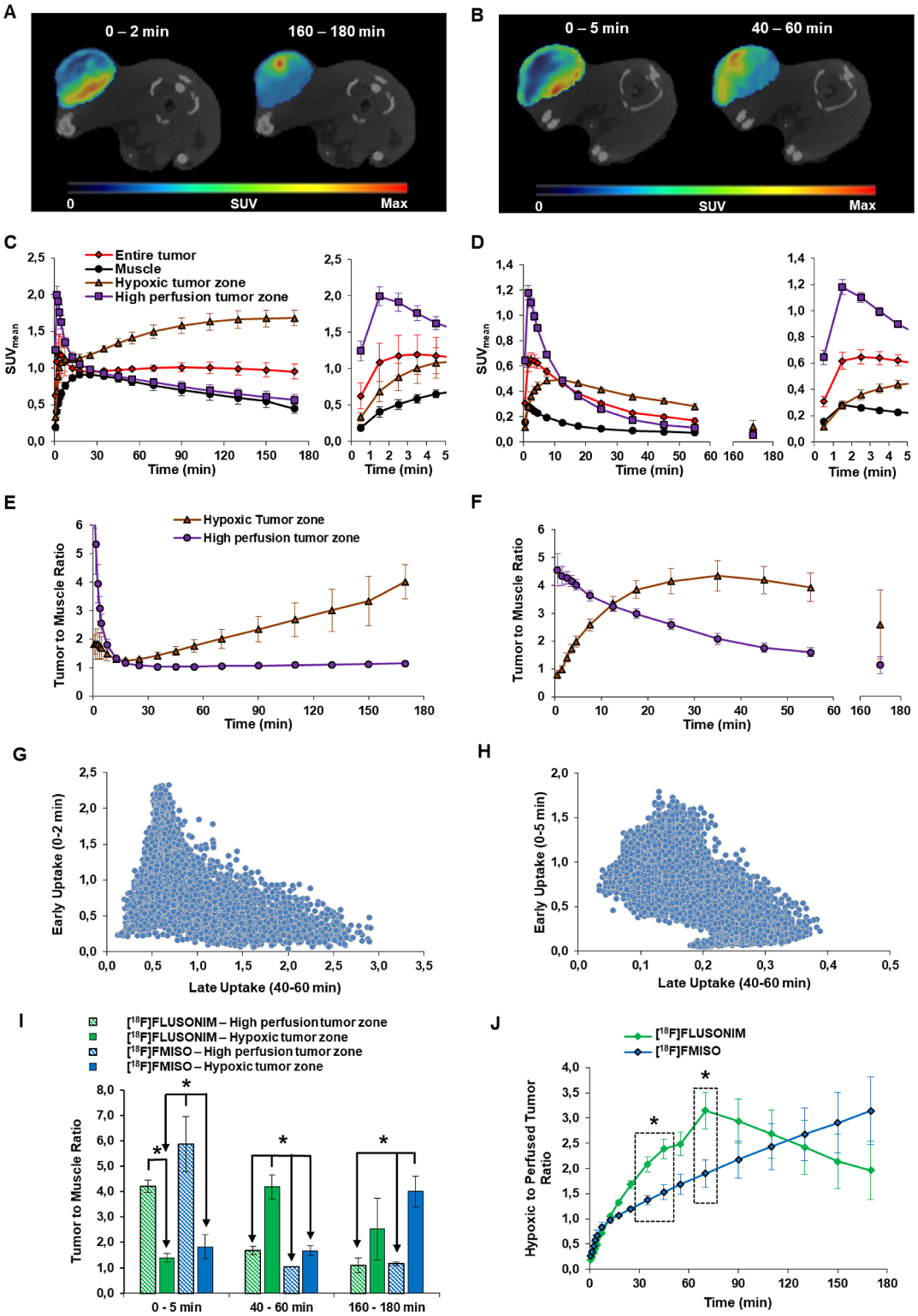

Figure 5. Perfusion vs hypoxia imaging in the rhabdomyosarcoma model ($n = 8$). Fused PET/CT images were hidden from elimination organs at early and late times for [^{18}F]FMISO (A) and for [^{18}F]FLUSONIM (B). TACs for [^{18}F]FMISO (C) and [^{18}F]FLUSONIM (D). TMRs for [^{18}F]FMISO (E) and [^{18}F]FLUSONIM (F). Voxel-by-voxel correlation between early (perfusion) and late (hypoxia) uptakes for [^{18}F]FMISO (G) and [^{18}F]FLUSONIM (H). Comparison of TMRs for [^{18}F]FLUSONIM and [^{18}F]FMISO (I, J).

stability of [^{18}F]FLUSONIM was consistent with its renal clearance, similar to what was observed for [^{18}F]HX4[14,15] and [^{18}F]DiFA.[23]

PET-CT Imaging Studies in Rhabdomyosarcoma Models

We evaluated the specificity of [^{18}F]FLUSONIM for hypoxia in the rhabdomyosarcoma WAG/Rij rat model[15] and compared it with [^{18}F]FLUSONIM and [^{18}F]FMISO in the same animals using a dynamic PET imaging schedule for 180 min. Each animal

https://doi.org/10.1021/jacsau.4c00546
JACS Au 2024, 4, 3248−3257

received a dose of [^{18}F]FLUSONIM and then [^{18}F]FMISO at intervals of 24 or 48 h. The data obtained from [^{18}F]FMISO PET imaging were totally consistent with literature results (Figure 4A).[15] [^{18}F]FMISO uptake was higher in the whole tumor compared to muscle (used as a reference healthy tissue) at all time points. The TAC for the whole tumor displayed a rapid entry in the early phase due to perfusion, followed by a slight decrease until approximately 20 min, and then by a plateau with SUV_{mean} around 1, indicating [^{18}F]FMISO retention in hypoxic cells. In contrast, the TAC for muscle showed a low progressive increase for the first 20 min, and then a negative slope to give SUV_{mean} of approximately 0.45 at 180 min post-injection in accordance with the slow clearance. Thus, tumor−muscle ratios (TMRs, calculated from SUV_{mean} values) increased progressively with time to reach only 2.6 at 180 min (Figure 4C). [^{18}F]FLUSONIM displayed different accumulation patterns compared to [^{18}F]FMISO (Figure 4B). The TACs for both whole tumor and muscle showed a rapid uptake of [^{18}F]FLUSONIM in the first 5 min, followed by a progressive decrease. The uptake levels (SUV_{mean}) in both tumor and muscle were lower for [^{18}F]FLUSONIM compared to [^{18}F]FMISO throughout the acquisition, in connection with the faster clearance of [^{18}F]FLUSONIM relative to [^{18}F]FMISO. However, the uptake differences between tumor and muscle were much higher for [^{18}F]FLUSONIM compared to [^{18}F]FMISO in the range of 15 to 60 min pi, especially at around 30 min corresponding to the maximal TMR of 3.4 (Figure 4C). This value was exceptionally high, indicating higher TMRs for [^{18}F]FLUSONIM compared to [^{18}F]FMISO and much shorter times after injection. It is noteworthy that [^{18}F]HX4 displayed similar TAC and TMR profiles compared to [^{18}F]FLUSONIM, but the time scale and the TMR values for [^{18}F]HX4 were far less advantageous.[15] These preliminary data foreshadowed [^{18}F]FLUSONIM as a promising radiopharmaceutical for hypoxia PET.

In order to further investigate the specific accumulation of the radiopharmaceuticals in hypoxic tumor regions, we distinguished between the early phase uptake, typical of tumor vascularization and perfusion, and accumulation in the later period characteristic of hypoxia (Figure 5)[32,33] As previously described in other tumor models,[32] the accumulation of [^{18}F]FMISO was located on the outer periphery of the tumor at early stages (0−2 min) and deeper within the tumor at later times (160−180 min) according to tumor heterogeneity (Figure 5A). [^{18}F]FLUSONIM displayed a similar pattern of accumulation, with the difference being the late phase occuring earlier (40−60 min) compared to [^{18}F]FMISO (Figure 5B). Figure 5 brings together the refined results for the comparison of the perfusion zone (early times) and hypoxia regions (late phase) for both [^{18}F]FMISO and [^{18}F]FLUSONIM in terms of TACs, TMRs, as well as hypoxic/perfused regions ratios (HPRs) and correlations. The TACs for the perfusion zone for both [^{18}F]FMISO and [^{18}F]FLUSONIM followed the expected pattern, indicating no specific retention, namely a rapid increase in the first minute followed by a sharp decrease (Figure 5C,D). As a consequence, the TMRs for the perfusion zone in function of time rapidly (from 25 min) dropped to 1 for [^{18}F]FMISO, indicating no significant contrast (Figure 5E). For [^{18}F]-FLUSONIM, TMRs reached 1 later (beyond 60 min) (Figure 5F). The difference in hydrophilicity between [^{18}F]FMISO and [^{18}F]FLUSONIM could explain this phenomenon. The TACs for the hypoxic zone were different for [^{18}F]FMISO and [^{18}F]FLUSONIM (Figure 5C, D). They reflected those of the whole tumor, corrected from the perfusion zone. Thus, TMRs slowly increased with time for [^{18}F]FMISO until reaching a value of approximately 4 at 180 min (Figure 5E), whereas TMRs over 4 were reached between 20 and 60 min for [^{18}F]-FLUSONIM (Figure 5F). A downward trend was observed in the correlation between early versus late uptakes for both [^{18}F]FMISO and [^{18}F]FLUSONIM (Figure 5H and G); and in all cases, the differences of TMRs between perfusion and hypoxic zones and between [^{18}F]FMISO and [^{18}F]FLUSONIM were statistically significant for the three time periods (0−5, 40−60, and 160−180 min) (Figure 5I). The evolution of HPRs in over time for [^{18}F]FLUSONIM and [^{18}F]FMISO was close to the curves of TMRs, with statistically significant differences noted between 30 and 60 min (Figure 5J). The overall findings supported specific properties of [^{18}F]FLUSONIM for hypoxia with unmatched performance in terms of imaging contrast and delay.

Histology and Autoradiography Studies

To confirm hypoxia specificity of [^{18}F]FLUSONIM, we performed *ex vivo* histology and autoradiography studies at 30 and 60 min post-injection to examine the relationship between [^{18}F]FLUSONIM accumulation and CA-IX hypoxia staining (Figure 6).[22,34,35] Hoechst coloration and hematoxylin and eosin staining of tumor sections were also performed to identify heterogeneity of tumors. Hoechst distribution was predominant in peripheral tumor regions typical of normoxic perfused zones with high nuclear densities (92.6 ± 1.6%). In the depths of the tumor, low nuclear density regions (32.2 ± 2.2%) were found and assigned to necrotic zones. Hypoxic areas were located at the interface where nuclear densities were intermediate (59.4 ± 2.7%). A similar repartition was mirrored in the hematoxylin and eosin image. CA-IX staining areas were observed in all tumor slices, with a heterogeneous distribution across the sections as previously reported for the rhabdomyosarcoma tumor model.[35]

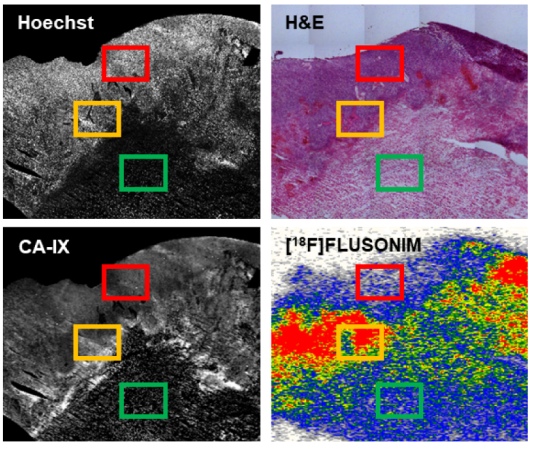

Region	Surface staining (%)		Radioactivity level (DLU.10^3/mm^2)	
	Hoechst	CA-IX	30 min	60 min
Normoxic	92.6±1.6	8.2±3.1	81.00±5.47	31.99±2.32
Hypoxic	59.4±2.7	20.5±1.3	162.37±9.19	75.38±5.01
Necrotic	30.2±2.2	NA	5.64±0.89	37.88±3.86

Figure 6. Histological, immunostaining, and autoradiography results for tumor sections of rhabdomyosarcoma rats.

https://doi.org/10.1021/jacsau.4c00546
JACS Au 2024, 4, 3248−3257

CA-IX staining was the highest (20.5 ± 1.3%) in identified hypoxic regions and low (8.2 ± 3.1%) in normoxic zones. Autoradiography images revealed a heterogeneous spatial distribution of radioactivity consistent with CA-IX staining. Hypoxic zones displayed a significantly higher uptake of [^{18}F]FLUSONIM than the normoxic and necrotic zones at both 30 and 60 min. Radioactivity levels were globally higher at 30 min than at 60 min, in agreement with uptake kinetics. Thus, the good correlation between autoradiography and immunohistochemistry was in agreement with the specific retention of [^{18}F]FLUSONIM in hypoxic tissues. It is noteworthy that under the same technical conditions, distribution of [^{18}F]FAZA in squamous carcinoma tumor sections was homogeneous for 30 min pi. Correlation between [^{18}F]FAZA distribution and density of hypoxic cells was significant only from 2 h pi.[36]

Radiometabolism Studies in Tumor

Tumors excised 60 min post-injection of [^{18}F]FLUSONIM were analyzed by radioHPLC. After treatment, we found that >85% of the radioactivity in the tumor homogenates was recovered in the low-molecular-weight fractions. The amount of radioactivity covalently binding to the macromolecule fraction was negligible. Similar results were found with [^{18}F]FMISO and [^{18}F]DiFA.[37] RadioHPLC analysis of the low-molecular-weight fraction revealed the formation of new radioactive products without any traces of [^{18}F]FLUSONIM (Figure 7). The

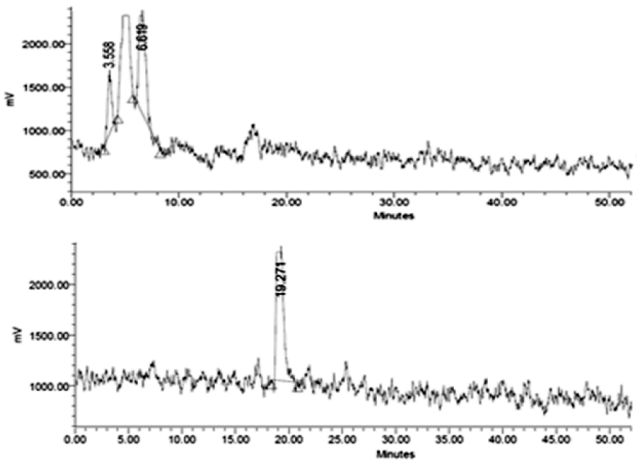

Figure 7. RadioHPLC of tumor extract at 60 min (top) vs [^{18}F]FLUSONIM from the quality control (bottom).

radiometabolites were more polar than the parent radiotracer, suggesting transformations according to the well-established reductive processes of the 2-nitroimidazolyl compounds in hypoxic cells.[2] Such a result further underscores the hypoxia specificity of [^{18}F]FLUSONIM.

CONCLUSION

Although a variety of ^{18}F-radiolabeled nitroimidazole derivatives have been successfully involved in hypoxia PET imaging for both preclinical and clinical applications, a novel radiopharmaceutical that gives high contrast images within short acquisition delay post-injection was still missing for both diagnostic and cancer therapy purposes. Here is described [^{18}F]FLUSONIM that was designed to contain a sulfo group to provide high hydrophilic properties and, consequently, a rapid clearance. High yielding radiosynthesis of [^{18}F]FLUSONIM was performed in a one-step process by radiofluorination of a sultone precursor easily obtained from commercially available products. [^{18}F]-FLUSONIM was shown to exhibit rapid clearance from healthy organs and rapid urinary elimination in accordance with its high hydrophilicity as well as high *in vivo* stability outside hypoxic conditions. More importantly, PET imaging studies in the rhabdomyosarcoma model combined with histology demonstrated that [^{18}F]FLUSONIM exhibited high specific uptake in hypoxic tumor regions at less than 60 min post-injection. Thus, hypoxia PET imaging using [^{18}F]FLUSONIM provided unprecedented performances in terms of TMRs and acquisition delays. The overall results unequivocally demonstrate that [^{18}F]FLUSONIM meets the criteria of an ideal candidate for hypoxia PET imaging, showing significant promise for preclinical and clinical applications. Current efforts are focused on extending [^{18}F]FLUSONIM PET imaging to other hypoxic cancers in view of clinical transfer.

MATERIALS AND METHODS

General Chemistry and Radiochemistry

Full descriptions of chemical and radiochemical syntheses, as well as the analytical techniques used, are provided in the Supporting Information. Unless otherwise noted, all reagents were obtained commercially and used without further purification. Fluorine-18 was generated at the Cyceron center.

Synthesis of FLUSONIM

FLUSONIM was synthesized in four steps from 2-nitroimidazole **2** (57% overall yield, gram scale). For detailed methods and the characterization of each compound, see the Supporting Information.

Radiosynthesis of [^{18}F]FLUSONIM

[^{18}F]Fluoride was produced via the ^{18}O(p,n)^{18}F nuclear reaction by irradiating ^{18}O- enriched water with an 18 MeV proton beam from an IBA Cyclone 18/9 cyclotron. At the end of bombardment, an aqueous solution of [^{18}F]fluoride was delivered to a TRACERlab FXFN module (GE). [^{18}F]fluoride was trapped on a Sep-Pak Light QMA and then eluted into the reaction vessel using 0.8 mL of a solution of potassium carbonate (K_2CO_3, 1.76 mg) and Kryptofix ($K_{2.2.2}$, 10.5 mg) in water (350 μL) and acetonitrile (450 μL). The resulting [^{18}F]KF/$K_{2.2.2}$/K_2CO_3 complex was dried by azeotropic distillation under vacuum and helium flow by heating at 90 °C for 10 min. Following the drying step of [^{18}F]fluoride, the sultone precursor **1** (5.2 mg) preliminarily dissolved in acetonitrile (1.2 mL) was added into the reaction vessel and heated at 110 °C for 15 min. After this time, the reactor was cooled to 45 °C and the crude reaction mixture was diluted with water (2 mL). [^{18}F]FLUSONIM was isolated by semipreparative HPLC (Macherey-Nagel Nucleodur C18 Pyramid column 5 μm, 10 × 250 mm; mobile phase: ethanol/NaH_2PO_4 (10 mM), 1:9; flow rate, 3 mL/min; λ = 280 nm). [^{18}F]FLUSONIM was collected between approximately 23−25 min in 5−7 mL fractions, ready to use for *in vivo* injection.

Log *P* and Log *D* Determination

The Log *P* and Log $D_{7.4}$ values were measured by using a standard shake flask method. Approximately 0.148 MBq of formulated [^{18}F]-FLUSONIM (10 μL, concentration of 14.8 MBq/mL) was added into a hemolysis tube containing a 1:1 mixture (2 mL) of water or phosphate buffer pH 7.4 (0.01 M) and 1-octanol. The hemolysis tube was shaken at 25 °C for 40 min and then centrifuged at 4000*g* for 5 min. Three aliquots (100 μL each) withdrawn from the organic and buffer layers were gamma-counted. The experiment was carried out in triplicate.

In Vitro Stability Studies

Formulated [^{18}F]FLUSONIM was incubated at 37 °C up to 180 min and then analyzed by radioHPLC. Aliquots of formulated [^{18}F]-FLUSONIM were also added to plasma samples from rats. After incubation at 37 °C up to 180 min, plasma samples were centrifuged (4024*g*, 10 min, 4 °C) and then analyzed by radioHPLC.

https://doi.org/10.1021/jacsau.4c00546
JACS Au 2024, 4, 3248−3257

Animal Experiments

The animal investigations were conducted in accordance with the current European directive (2010/63/EU) as incorporated into national legislations, and protocols were approved by the French (#10773) and Belgian (UCL/2014/MD/026) committees on animal ethics. *In vivo* experiments were performed using healthy male Wistar rats (309 ± 19 g, n = 10, in-house breeding stock) and rhabdomyosarcoma tumor-bearing male adult WAG/Rij rats (226 ± 17 g before implantation, n = 11, Charles River). Tumor implantations were performed under anesthesia with a mixed solution of ketamine and xylazine at a dose of 80 and 10 mg/kg, respectively, as previously described.[38] All animals were housed in groups of two or more under a 12-h light/12-h dark cycle with access to food and water ad libitum. The general condition of the animals was monitored daily, and tumor growth was measured 3 times per week with a caliper. Rats were included in the study when tumor reached a volume of 3 cm^3 (width × length^2 × $\pi/6$) to ensure reproducible degree of hypoxia.[36]Tumor follow-up was terminated before reaching the ethical end point of 10% of the body weight.[39] Animals were maintained under isoflurane anesthesia throughout all experimental procedures (induction, 5%; maintenance, around 2.5%, with 70% N_2O/30% O_2). Body temperature was maintained close to 37.5 °C using a feedback controlled system, and a catheter was inserted into the tail vein for radiotracer administration ([^{18}F]FMISO: 23.7 ± 2.5 MBq; [^{18}F]FLUSONIM: 23.2 ± 3.0 MBq). Animals were euthanized at the end of the procedure by decapitation under deep anesthesia (isoflurane 5%).

In Vivo Stability Studies

Stability of [^{18}F]FLUSONIM in blood was checked at 15, 30, 60, and 150 min post-injection. Blood samples (≈ 2.5 mL) were collected via intracardiac puncture, heparinized, and centrifuged (4024*g*, 5 min, 4 °C). Plasma was then separated, mixed with an equivalent volume of acetonitrile, and centrifuged again (4024*g*, 10 min, 4 °C). Supernatants were filtered (0.45 μm PVDF), concentrated under nitrogen flow at 40 °C, and then analyzed by semipreparative radioHPLC. Each samples were weighted, and the radioactivity was counted at different stages, before and after centrifugation and filtration (Cobra 2 Gamma counter, PerkinElmer). Acetonitrile extraction yields were about 85% and filtration yields were >95%.

PET-CT Imaging

Imaging experiments were developed using an Inveon μPET/CT scanner (Siemens Healthcare Molecular Imaging). Scans were performed with an emphasis on the abdomen. Respiratory rate was monitored during imaging sessions to ensure a stable and reproducible anesthesia from one animal to another and between successive acquisitions. Simultaneous injection of radiotracer and initiation of PET acquisition were performed, data were acquired in list-mode, and PET images were reconstructed using iterative OSEM3D/MAP algorithm. Dead-time, random, scatter, and attenuation correction (based on CT) were applied. Image analysis was performed with p-Mod 3.7 software (p-MOD Technologies). Briefly, PET and CT images were coregistered and volumes of interest (VOIs) were semiautomatically delimitated on the following organs: heart, lung, liver, muscle, bone, kidney, entire bladder, and entire tumor, if available. Time activity curves (TAC) were extracted from PET images and normalized as the Standardized Uptake Value (SUV). Data were expressed as SUV_{mean}, and tumor-to-muscle ratios (TMRs) were calculated from mean values (see the Supporting Information for data expressed as SUV_{max}).

Microdissection

After imaging, animals were euthanized by decapitation under deep anesthesia (isoflurane 5%). Tumors as well as organs such as brain, muscle, blood, plasma, heart, lung, liver, and bone were dissected. Samples were weighed, and the radioactivity was measured in a γ-counter (Cobra 2 Gamma counter, PerkinElmer). Some tumors were divided and immediately frozen for autoradiographic studies.

Autoradiography and Fluorescence Microscopy

Tumor pieces were rapidly frozen by immersion in −40 °C isopentane (Sigma-Aldrich) and sectioned in a cryostat (Leica CM3050; 20 μm thick slices). The slices were immediately exposed overnight to high-performance storage phosphor screens, which were then scanned in a Phosphor Imager Scanner (Cyclone; Perkin−Elmer, pixel size: 43.2 × 43.2 μm^2). Phosphor imaging plates were read at a pixel resolution of 50 μm. After autoradiographic exposure, the same or adjacent frozen sections were stained with Mayer's hematoxylin and eosin (H&E; Sigma-Aldrich). High-magnification images were imaged by light microscopy (x50; Leica DMi8, pixel size: 1.3 × 1.3 μm^2), generating paired data from H&E staining and digital autoradiograms. Remaining adjacent slices were stored at −20 °C until immunofluorescent staining. Slices were first pretreated by blocking the nonspecific binding (0.3% Triton x100, and 3% bovine serum albumin (BSA) in phosphate buffer saline (PBS) for 2 h at room temperature). Slices were then incubated overnight with primary antibodies (Rabbit polyclonal Anti-CA-IX antibody, 1.0 μg/mL, Novus Biological) with 0.3% Triton and 1% BSA in PBS at 4 °C, followed by incubation at room temperature for 2 h with fluorophore-labeled secondary antibodies (Donkey antirabbit IgG conjugated with Alexa-Fluor 488, 10 μg/mL, Invitrogen). The cell nuclei were counterstained with Hoechst 33342 (20 μg/mL, Sigma-Aldrich). High-resolution images were acquired (×50; Leica DMi8 fluorescence microscope, pixel size: 1.3 × 1.3 μm). These virtual slices (n = 12) were then processed with ImageJ 1.51 software (http://imagej.nih.gov/ij/) to quantify the Nuclear density ("Hoechst staining surface"/"Total tissue surface" %) and the Hypoxic fraction ("CA-IX staining surface"/"Total tissue surface" %). Regions of interest (ROI) were manually delineated to identify hypoxic (high density of CA-IX staining), necrotic (low density of CA-IX staining and low nuclear density), and normoxic zones (low density of CA-IX staining and high nuclear density). Same ROIs were then applied to digital autoradiograms with OptiQuant version 05.00 software (Packard Instrument Co.). The optical quantification of radioactive slices was expressed in digital light units per square millimeter (DLU.mm^2) for ROI, with the subtraction of background autoradiogram signals.

Tumor Metabolites Analysis

After excision, tumor pieces were crushed in acetonitrile (1 mL per gram of tumor) and centrifuged (4024*g*, 10 min, 4 °C). The supernatants containing 80% of the initial tumor piece radioactivity were filtered (0.45 μm PVDF). 95% of the radioactivity was recovered after filtration. The samples were then concentrated under nitrogen flow at 40 °C and analyzed by semipreparative radioHPLC. The radioactivity of weighted samples was measured at different stages to control process efficiency. Acetonitrile extraction yields were close to 90% for plasma and 80% for tumor, and filtration yields were greater than 95%.

Data Analysis

Data were reported as mean values ± standard error of the mean (SEM). Statistical data analysis was performed using a "one-way ANOVA" followed by Tukey's test with Prism 4.0 (GraphPad Software, USA). P-values of <0.05 were considered statistically significant.

■ ASSOCIATED CONTENT

Supporting Information

The Supporting Information is available free of charge at https://pubs.acs.org/doi/10.1021/jacsau.4c00546.

Detailed chemical synthesis description, ^{1}H, ^{13}C, and ^{19}F NMR spectra, supplementary data, and figures (PDF)

■ AUTHOR INFORMATION

Corresponding Author

Cécile Perrio − *CNRS, CEA, Normandie Univ, UNICAEN, Cyceron, Caen 14074, France;* orcid.org/0000-0001-6559-3861; Email: perrio@cyceron.fr

https://doi.org/10.1021/jacsau.4c00546
JACS Au 2024, 4, 3248−3257

Authors

Clémence Maingueneau − *CNRS, CEA, Normandie Univ, UNICAEN, Cyceron, Caen 14074, France*
Anne-Elodie Lafargue − *CNRS, CEA, Normandie Univ, UNICAEN, Cyceron, Caen 14074, France*
Stéphane Guillouet − *CNRS, CEA, Normandie Univ, UNICAEN, Cyceron, Caen 14074, France*
Fabien Fillesoye − *CNRS, CEA, Normandie Univ, UNICAEN, Cyceron, Caen 14074, France*
Thanh T. Cao Pham − *UCLouvain, Biomedical Magnetic Resonance Unit (REMA), Woluwe-Saint-Lambert 1200, Belgium*
Bénédicte F. Jordan − *UCLouvain, Biomedical Magnetic Resonance Unit (REMA), Woluwe-Saint-Lambert 1200, Belgium*

Complete contact information is available at: https://pubs.acs.org/10.1021/jacsau.4c00546

Notes

The authors declare no competing financial interest.

■ ACKNOWLEDGMENTS

This work was supported by CNRS, Région Normandie, Caen University, CEA and Labex IRON (ANR-11-LABX-0018-01). The authors thank the cyclotron operators Mr. Tirel and Mr. Delamare for [^{18}F]fluoride production, and Mr. Saulnier for radiotracer injection. B.F. Jordan is F.R.S./FNRS Research Director.

■ REFERENCES

(1) Muz, B.; de la Puente, P.; Azab, F.; Azab, A. K. The Role of Hypoxia in Cancer Progression, Angiogenesis, Metastasis, and Resistance to Therapy. *Hypoxia* **2015**, *3*, 83−92.
(2) Challapalli, A.; Carroll, L.; Aboagye, E. O. Molecular Mechanisms of Hypoxia in Cancer. *Clin Transl Imaging* **2017**, *5*, 225−253.
(3) Bigos, K. J.; Quiles, C. G.; Lunj, S.; Smith, D. J.; Krause, M.; Troost, E. G.; West, C. M.; Hoskin, P.; Choudhury, A. Tumour response to hypoxia: understanding the hypoxic tumour microenvironment to improve treatment outcome in solid tumours. *Front. Oncol.* **2024**, *14*, 1331355.
(4) Busk, M.; Overgaard, J.; Horsman, M. R. Imaging of Tumor Hypoxia for Radiotherapy: Current Status and Future Directions. *Semin Nucl. Med.* **2020**, *50*, 562−583.
(5) Grimes, D. R.; Warren, D. R.; Warren, S. Hypoxia Imaging and Radiotherapy: Bridging the Resolution Gap. *Br J Radiol.* **2017**, *90*, 20160939.
(6) Stieb, S.; Eleftheriou, A.; Warnock, G.; Guckenberger, M.; Riesterer, O. Longitudinal PET Imaging of Tumor Hypoxia during the Course of Radiotherapy. *Eur. J. Nucl. Med. Mol. Imaging* **2018**, *45*, 2201−2217.
(7) Bonnitcha, P.; Grieve, S.; Figtree, G. Clinical Imaging of Hypoxia: Current Status and Future Directions. *Free Radic. Biol. Med.* **2018**, *126*, 296−312.
(8) Fleming, I. N.; Manavaki, R.; Blower, P. J.; West, C.; Williams, K. J.; Harris, A. L.; Domarkas, J.; Lord, S.; Baldry, C.; Gilbert, F. J. Imaging tumour hypoxia with positron emission tomography. *Br. J. Cancer* **2015**, *112*, 238−250.
(9) Nguyen, A. T.; Kim, H. K. Recent Developments in PET and SPECT Radiotracers as Radiopharmaceuticals for Hypoxia Tumors. *Pharmaceutics* **2023**, *15*, 1840.
(10) Saxena, P.; Gambhir, S.; Dixit, M. Insight into Tumor Hypoxia: Radionuclide-based Biomarker as Diagnostic Tools. *Curr. Top. Med. Chem.* **2023**, *23*, 1136−1154.
(11) Hirata, K.; Watanabe, S.; Kitagawa, Y.; Kudo, K. A Review of Hypoxia Imaging Using ^{18}F-Fluoromisonidazole Positron Emission Tomography. *Methods Mol. Biol.* **2024**, *2755*, 133−140.
(12) Xu, Z.; Li, X.-F.; Zou, H.; Sun, X.; Shen, B. ^{18}F-Fluoromisonidazole in Tumor Hypoxia Imaging. *Oncotarget* **2017**, *8*, 94969−94979.
(13) Thorwarth, D.; Mönnich, D.; Zips, D. Methodological aspects on hypoxia PET acquisition and image processing. *Q J. Nucl. Med. Mol. Imaging* **2013**, *57* (3), 235−243.
(14) Dubois, L. J.; Lieuwes, N. G.; Janssen, M. H. M.; Peeters, W. J. M.; Windhorst, A. D.; Walsh, J. C.; Kolb, H. C.; Öllers, M. C.; Bussink, J.; van Dongen, G. A. M. S.; et al. Preclinical Evaluation and Validation of [^{18}F]HX4, a Promising Hypoxia Marker for PET Imaging. *Proc. Natl. Acad. Sci. U. S. A.* **2011**, *108*, 14620−14625.
(15) Peeters, S. G. J. A.; Zegers, C. M. L.; Lieuwes, N. G.; van Elmpt, W.; Eriksson, J.; van Dongen, G. A. M. S.; Dubois, L.; Lambin, P. A Comparative Study of the Hypoxia PET Tracers [^{18}F]HX4, [^{18}F]FAZA, and [^{18}F]FMISO in a Preclinical Tumor Model. *Int. J. Radiat. Oncol. Biol. Phys.* **2015**, *91*, 351−359.
(16) Peeters, S. G. J. A.; Zegers, C. M. L.; Biemans, R.; Lieuwes, N. G.; van Stiphout, R. G. P. M.; Yaromina, A.; Sun, J. D.; Hart, C. P.; Windhorst, A. D.; van Elmpt, W.; et al. TH-302 in Combination with Radiotherapy Enhances the Therapeutic Outcome and Is Associated with Pretreatment [^{18}F]HX4 Hypoxia PET Imaging. *Clin. Cancer Res.* **2015**, *21*, 2984−2992.
(17) Sanduleanu, S.; Hamming-Vrieze, O.; Wesseling, F. W. R.; Even, A. J. G.; Hoebers, F. J.; Hoeben, A.; Vogel, W. V.; Tesselaar, M. E. T.; Parvin, D.; Bartelink, H.; et al. [^{18}F]-HX4 PET/CT Hypoxia in Patients with Squamous Cell Carcinoma of the Head and Neck Treated with Chemoradiotherapy: Prognostic Results from two Prospective Trials. *Clin. Transl. Radiat. Oncol.* **2020**, *23*, 9−15.
(18) Sanduleanu, S.; Wiel, A. M. A. V.; Lieverse, R. I. Y.; Marcus, D.; Ibrahim, A.; Primakov, S.; Wu, G.; Theys, J.; Yaromina, A.; Dubois, L. J.; et al. Hypoxia PET Imaging with [^{18}F]-HX4-A Promising Next-Generation Tracer. *Cancers* **2020**, *12*, 1322.
(19) Betts, H. M.; O'Connor, R. A.; Christian, J. A.; Vinayakamoorthy, V.; Foweraker, K.; Pascoe, A. C.; Perkins, A. C. Hypoxia Imaging with [^{18}F]HX4 PET in Squamous Cell Head and Neck Cancers: A Pilot Study for Integration into Treatment Planning. *Nucl. Med. Commun.* **2019**, *40*, 73−78.
(20) Zegers, C. M.; Hoebers, F. J.; van Elmpt, W.; Bons, J. A.; Öllers, M. C.; Troost, E. G.; Eekers, D.; Balmaekers, L.; Arts-Pechtold, M.; Mottaghy, F. M.; et al. Evaluation of Tumour Hypoxia during Radiotherapy using [^{18}F]HX4 PET Imaging and Blood Biomarkers in Patients with Head and Neck Cancer. *Eur. J. Nucl. Med. Mol. Imaging* **2016**, *43*, 2139−2146.
(21) Chen, L.; Zhang, Z.; Kolb, H. C.; Walsh, J. C.; Zhang, J.; Guan, Y. ^{18}F-HX4 Hypoxia Imaging with PET/CT in Head and Neck Cancer: A comparison with ^{18}F-FMISO. *Nucl. Med. Commun.* **2012**, *33*, 1096−1102.
(22) Carlin, S.; Zhang, H.; Reese, M.; Ramos, N. N.; Chen, Q.; Ricketts, S. A. A Comparison of the Imaging Characteristics and Microregional Distribution of 4 Hypoxia PET Tracers. *J. Nucl. Med.* **2014**, *55*, 515−521.
(23) Nakata, N.; Kiriu, M.; Okumura, Y.; Zhao, S.; Nishijima, K.-I.; Shiga, T.; Tamaki, N.; Kuge, Y.; Matsumoto, H. Comparative Evaluation of [^{18}F]DiFA and its Analogs as Novel Hypoxia Positron Emission Tomography and [^{18}F]FMISO as the Standard. *Nucl. Med. Biol.* **2019**, *70*, 39−45.
(24) Watanabe, S.; Shiga, T.; Hirata, K.; Magota, K.; Okamoto, S.; Toyonaga, T.; Higashikawa, K.; Yasui, H.; Kobayashi, J.; Nishijima, K.-I.; et al. Biodistribution and Radiation Dosimetry of the Novel Hypoxia PET Probe [^{18}F]DiFA and Comparison with [^{18}F]FMISO. *EJNMMI Res.* **2019**, *9*, 60.
(25) Goud, N. S.; Joshi, R. K.; Bharath, R. D.; Kumar, P. Fluorine-18: A Radionuclide with Diverse Range of Radiochemistry and Synthesis Strategies for Target Based PET Diagnosis. *Eur. J. Med. Chem.* **2020**, *187*, 111979.

(26) Wang, Y.; Lin, Q.; Shi, H.; Cheng, D. Fluorine-18: Radiochemistry and Target-Specific PET Molecular Probes Design. *Front. Chem.* **2022**, *10*, 884517.
(27) Schmitt, S.; Bouteiller, C.; Barré, L.; Perrio, C. Sultone Opening with [^{18}F]Fluoride: An Efficient 18F-Labelling Strategy for PET Imaging. *Chem. Commun.* **2011**, *47*, 11465−11467.
(28) Han, D. K.; Park, K. D.; Kim, Y. H. Sulfonated poly(ethylene oxide)-grafted polyurethane copolymer for biomedical applications. *J. Biomater. Sci., Polym. Ed.* **1998**, *9*, 163−174.
(29) Log P and Log D values for [^{18}F]DIFA have not been reported.
(30) Bonnet, M.; Hong, C. R.; Gu, Y.; Anderson, R. F.; Wilson, W. R.; Pruijn, F. B.; Wang, J.; Hicks, K. O.; Hay, M. P. Novel Nitroimidazole Alkylsulfonamides as Hypoxic Cell Radiosensitisers. *Bioorg. Med. Chem.* **2014**, *22*, 2123−2132.
(31) Beaufrez, J.; Guillouet, S.; Seimbille, Y.; Perrio, C. S. Synthesis, Fluorine-18 Radiolabeling, and In Vivo PET Imaging of a Hydrophilic Fluorosulfotetrazine. *Pharmaceuticals* **2023**, *16* (5), 636.
(32) Cho, H. J.; Ackerstaff, E.; Carlin, S.; Lupu, M. E.; Wang, Y.; Rizwan, A.; O'Donoghue, J.; Ling, C. C.; Humm, J. L.; Zanzonico, P. B.; et al. Noninvasive Multimodality Imaging of the Tumor Microenvironment: Registered Dynamic Magnetic Resonance Imaging and Positron Emission Tomography Studies of a Preclinical Tumor Model of Tumor Hypoxia. *Neoplasia* **2009**, *11*, 247−259.
(33) Busk, M.; Munk, O. L.; Jakobsen, S. S.; Horsman, M. R. Hypoxia Positron Emission Tomography Imaging: Combining Information on Perfusion and Tracer Retention to Improve Hypoxia Specificity. *Acta Oncol.* **2017**, *56*, 1583−1590.
(34) Dubois, L.; Peeters, S. G. J. A.; van Kuijk, S. J. A.; Yaromina, A.; Lieuwes, N. G.; Saraya, R.; Biemans, R.; Rami, M.; Parvathaneni, N. K.; Vullo, D.; et al. Targeting Carbonic Anhydrase IX by Nitroimidazole Based Sulfamides Enhances the Therapeutic Effect of Tumor Irradiation: A New Concept of Dual Targeting Drugs. *Radiother Oncol.* **2013**, *108*, 523−528.
(35) Dubois, L.; Landuyt, W.; Haustermans, K.; Dupont, P.; Bormans, G.; Vermaelen, P.; Flamen, P.; Verbeken, E.; Mortelmans, L. Evaluation of Hypoxia in an Experimental Rat Tumour Model by [(18)F]-Fluoromisonidazole PET and Immunohistochemistry. *Br. J. Cancer* **2004**, *91*, 1947−1954.
(36) Busk, M.; Horsman, M. R.; Jakobsen, S.; Hansen, K. V.; Bussink, J.; van der Kogel, A.; Overgaard, J. Can Hypoxia-PET Map Hypoxic Cell Density Heterogeneity Accurately in an Animal Tumor Model at a Clinically Obtainable Image Contrast? *Radiother Oncol.* **2009**, *92*, 429−436.
(37) Shimizu, Y.; Zhao, S.; Yasui, H.; Nishijima, K.-I.; Matsumoto, H.; Shiga, T.; Tamaki, N.; Ogawa, M.; Kuge, Y. A Novel PET Probe [^{18}F]DiFA Accumulates in Hypoxic Region via Glutathione Conjugation Following Reductive Metabolism. *Mol. Imaging Biol.* **2019**, *21*, 122−129.
(38) Tran, L.-B.-A.; Bol, A.; Labar, D.; Jordan, B.; Magat, J.; Mignion, L.; Grégoire, V.; Gallez, B. Hypoxia Imaging with the Nitroimidazole ^{18}F-FAZA PET Tracer: A Comparison with OxyLite, EPR Oximetry and ^{19}F-MRI Relaxometry. *Radiother Oncol.* **2012**, *105*, 29−35.
(39) Workman, P; Aboagye, E O; Balkwill, F; Balmain, A; Bruder, G; Chaplin, D J; Double, J A; Everitt, J; Farningham, D A H; Glennie, M J; Kelland, L R; Robinson, V; Stratford, I J; Tozer, G M; Watson, S; Wedge, S R; Eccles, S A Guidelines for the Welfare and Use of Animals in Cancer Research. *Br. J. Cancer* **2010**, *102*, 1555−1577.

https://doi.org/10.1021/jacsau.4c00546
JACS Au 2024, 4, 3248−3257